

Proposal for asymmetric photoemission and tunneling spectroscopies in quantum simulators of the triangular-lattice Fermi-Hubbard model

Shuai A. Chen,¹ Qianqian Chen,² and Zheng Zhu^{2,3,*}

¹Department of Physics, Hong Kong University of Science and Technology, Clear Water Bay, Hong Kong, China

²Kavli Institute for Theoretical Sciences, University of Chinese Academy of Sciences, Beijing 100190, China

³CAS Center for Excellence in Topological Quantum Computation, University of Chinese Academy of Sciences, Beijing, 100190, China

(Dated: September 15, 2022)

Recent realization of well-controlled quantum simulators of the triangular-lattice Fermi-Hubbard model, including the triangular optical lattices loaded with ultracold Fermions and the heterostructures of the transition-metal dichalcogenides, as well as the more advanced techniques to probe them, pave the way for studying frustrated Fermi-Hubbard physics. Here, we theoretically predict asymmetric photoemission and tunneling spectroscopies for a lightly hole-doped and electron-doped triangular Mott antiferromagnet, and reveal two distinct types of magnetic polarons: a *lightly* renormalized quasiparticle with the same momentum as the spin background and a *heavily* renormalized quasiparticle with a shifted momentum and a nearly flat band, using both analytical and unbiased numerical methods. We propose these theoretical findings to be verified in frustrated optical lattices and Moiré superlattices by probing various observables including the spectral function, the density of states, the energy dispersion and the quasiparticle weight. Moreover, we reveal the asymmetric response of the spin background against charge doping, demonstrating that the interplay between the local spin and charge degrees of freedom plays a vital role in doped triangular Mott antiferromagnets.

I. INTRODUCTION

The Fermi-Hubbard model is widely believed to be a prototypical model to capture the essential physics of many realistic strongly correlated systems, notably the doped Mott insulators [1]. Important insights into the doped Mott insulators could be gained by investigating the motion of the doped single charge and its interplay with the spin background. Due to its potential relevance to the high T_c cuprates [2, 3], such an issue has been extensively studied on the square lattice [4] and the interplay between spin and charge has been proved to play an essential role [5–17]. Nevertheless, those analogous problems on the triangular lattice, which are equally important and likely to exhibit distinct physics due to the geometric frustrations and the absence of particle-hole symmetry, still need plenty of endeavors. Recently, quantum simulating the Fermi-Hubbard model has been realized in both cold-atom optical lattices [18–38] and condensed-matter Moiré superlattices [39, 40], and the theoretical predictions can thereby be verified.

Compared with the complicated condensed-matter materials [39, 40], the optical lattice, which is a more controlled and pristine platform, has been remarkably advanced [18–38], where the momentum-resolved spin structure factor [33], the spectral function [36, 37] and the real-space motion of doped holes [34, 35] can be probed using high-resolution techniques. In particular, more recently, the triangular optical lattice loaded with ultracold Fermions has been implemented experimentally [24], as illustrated in Fig. 1(a), where the coupling strength U and the hopping amplitude t could be accurately tuned through Feshbach resonance [41] and the strength of the optical lattice [38], respectively. It is possi-

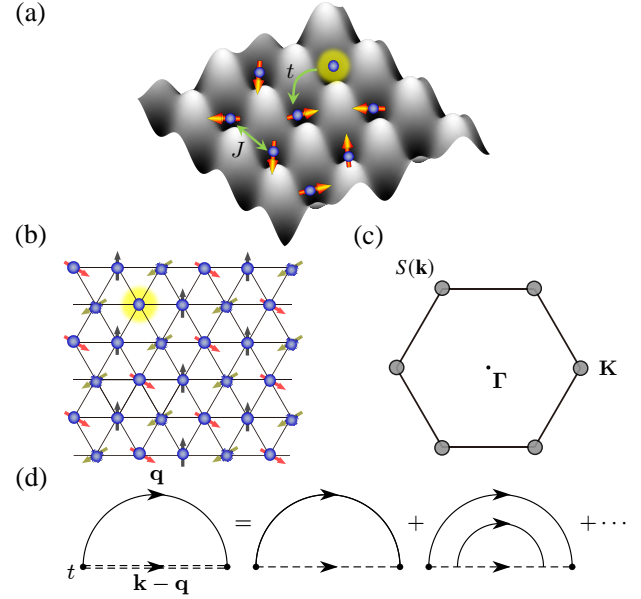


Fig. 1. (Color online.) (a) Fermions trapped in a triangular optical lattice. A 120° antiferromagnetic order emerges with a characteristic energy scale J , and it further dresses a bare hole with a cloud of magnons. (b) Schematic diagram of triangular Mott antiferromagnet with a single doped charge. (c) Schematic diagram of the static spin structure factor $S(\mathbf{k})$ for the 120° Néel order at half filling. The maxima of $S(\mathbf{k})$ are denoted by solid gray circles. (d) The rainbow diagram for SCBA calculations. Holon and magnon are presented by solid and dashed lines, respectively. The double dashed line represents the exact holon propagator. The vertex marked by the black dot is of order t .

ble to precisely track the motion of a single charge and obtain its interplay with fluctuating spin backgrounds [34, 35] due to a revolutionary real-space detection using quantum microscopy [18] that images the dynamics of all ultracold atoms

* zhuzheng@ucas.ac.cn

simultaneously and the angle-resolved photoemission spectroscopy (ARPES) that measures spectral function [36, 37].

In a different context, the transition-metal dichalcogenide (TMD) and its heterostructures, such as WSe_2/WS_2 hetero-bilayers [39], provide a distinct platform to simulate the triangular-lattice Hubbard model [39, 40] with widely tunable parameters like the charge carrier density [42–45], and advanced measurement techniques, such as the spectral functions and density of states by nano-ARPES [46] and scanning tunneling microscope (STM).

Nevertheless, it is highly controversial for previous studies on the fate of injected charges in a triangular Mott antiferromagnet [47–51] even for those with the same method like self-consistent Born approximation (SCBA) [47, 48] (details see Appendix). Therefore, resolving this critical problem is a much-needed task both theoretically and experimentally. Motivated by the above aspects, in this paper, we propose the photoemission and tunneling spectroscopies of lightly hole-doped and electron-doped triangular Mott antiferromagnet. By establishing the magnetic polaron theory analytically with self-consistent Born approximation (SCBA), we theoretically predict the asymmetric photoemission and tunneling spectroscopies with respect to the particle-hole transformation, and identify two distinct types of magnetic polarons: a lightly renormalized quasiparticle with the same momentum as the spin background and a heavily renormalized quasiparticle with a shifted momentum and nearly flat band, which implies even richer physics as compared to the square lattice. The density matrix renormalization group (DMRG) simulation, which resolves the sharp ambiguity from small size effect [47, 48] in the exact diagonalization (ED) method, numerically backs up the analytical conclusions. We further show the asymmetric responses of the spin background against charge doping concentration and demonstrate the validity of our theory at light doping. We remark that the signature of the asymmetry proposed here, including the spectral function, the density of states, and the static spin structure factor, can be directly probed in recently realized frustrated optical lattices and TMD hetero-bilayers.

II. MODEL HAMILTONIAN

The motion of the doped charge in a triangular lattice can be described by the Fermion-Hubbard model

$$H = -t \sum_{\langle ij \rangle \sigma} (c_{i\sigma}^\dagger c_{j\sigma} + h.c.) + U \sum_i n_{i\uparrow} n_{i\downarrow}, \quad (1)$$

where $c_{i\sigma}^\dagger$ ($c_{i\sigma}$) and n_i denote a fermion creation (annihilation) and particle number operators at site i , respectively. The summation runs over all the nearest-neighbor links $\langle ij \rangle$. In this work, we focus on the strong coupling regime, where the Hamiltonian at half-filling reduces to a pure Heisenberg spin model with the superexchange coupling $J = 4t^2/U$ and 120° Néel order in the ground state [52–55]. Upon doping a charge, i.e., $\sum_i n_i = N - 1$ (N the number of the lattice sites), the hopping process is triggered with amplitude t . Then the low-

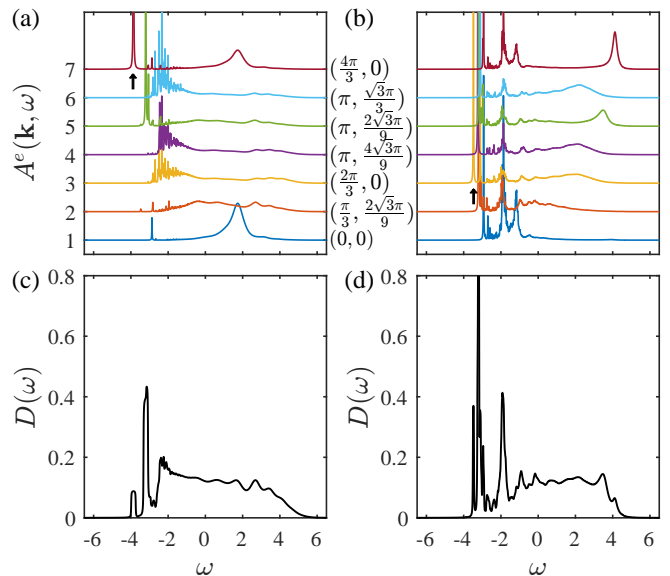


Fig. 2. (Color online.) The spectral function $A^e(\mathbf{k}, \omega)$ [(a) and (b)] and density of states $D(\omega)$ [(c) and (d)] obtained from SCBA at $N = 6 \times 6$ lattice with periodic boundary conditions. A well-defined quasiparticle peak (marked by black arrows) lies at the bottom of spectrum with $\mathbf{K} = (\frac{4\pi}{3}, 0)$ for $t/J = 5$ in (a) and $(\frac{2\pi}{3}, 0)$ for $t/J = -5$ in (b), respectively. The density of states $D(\omega)$ features a vanishing gap in a continuum limit for both sides, and for $t/J = -5$ in (d), it shows the divergent behavior. Here we set $|t| = 1$ as the unity of energy, and $\Delta\omega = 0.01$.

energy effective Hamiltonian reads

$$H = -t\mathcal{P} \sum_{\langle ij \rangle \sigma} (c_{i\sigma}^\dagger c_{j\sigma} + h.c.)\mathcal{P} + J \sum_{\langle ij \rangle} \mathbf{S}_i \cdot \mathbf{S}_j, \quad (2)$$

where \mathcal{P} projects to the single-occupancy subspace i.e. $n_i \leq 1$ and \mathbf{S}_i is a spin operator $\mathbf{S}_i = \frac{1}{2}c_i^\dagger(\sigma_x, \sigma_y, \sigma_z)c_i$ with $\sigma_{x,y,z}$ being Pauli matrices and $c_i = [c_{i\uparrow}, c_{i\downarrow}]^T$. Unlike the bipartite square-lattice case [5–10, 13–17, 56, 57], the particle-hole symmetry is absent here with the physics depending on the sign of hopping amplitude t [58]. We therefore perform a comparative study for $t > 0$ and $t < 0$, which can be connected by a full particle-hole transformation for both spins (see Appendix). We are devoted to light doping exemplified by a single charge doping with the methods of the SCBA [7, 8, 47, 48] and DMRG [59, 60].

III. MAGNETIC POLARON THEORY

We start from the half-filled spin background with an in-plane order, here the 120° Néel order is characterized by momentum $\mathbf{Q} = \mathbf{K}$ for the triangular Mott antiferromagnets [52–55]. We consider the order in XZ-plane and an in-plane rotation of each spin at \mathbf{r}_i by an angle $\mathbf{Q} \cdot \mathbf{r}_i$. Implementing the Holstein-Primakoff transformation with $S_i^z = S - a_i^\dagger a_i$, $S_i^+ = a_i$, we introduce a boson a to describe the low-

energy magnon excitations and get the Hamiltonian $H_a = \sum_{\mathbf{k}} \omega_{\mathbf{k}}^s \beta_{\mathbf{k}}^\dagger \beta_{\mathbf{k}}$, where $\omega_{\mathbf{k}}^s = \frac{\nu}{2} JS \sqrt{(1-\gamma_{\mathbf{k}})(1+2\gamma_{\mathbf{k}})}$ denotes the energy dispersion of magnons and the canonical modes $\beta_{\mathbf{k}} = u_{\mathbf{k}} a_{\mathbf{k}} - v_{\mathbf{k}} a_{-\mathbf{k}}^\dagger$. Here $\gamma_{\mathbf{k}} = \sum_{\delta} e^{i\mathbf{k}\cdot\delta} / \nu$ sums over all the $\nu = 6$ nearest-neighbor sites on the triangular lattice and $u_{\mathbf{k}}, v_{\mathbf{k}}$ are usual Bogoliubov factors in spin-wave theory. Then the rotated ground state can be constructed as $|\Psi_0\rangle = \exp(-\sum_{\mathbf{k}} \frac{v_{\mathbf{k}}}{u_{\mathbf{k}}} a_{\mathbf{k}} a_{-\mathbf{k}}) |\text{Néel}\rangle$.

Upon doping, the motion of the charge is dressed by magnons, forming a magnetic polaron. The creation of a spinless charge is described by h_i^\dagger in the fractionalization scheme: $c_{i\uparrow} = h_i^\dagger$ and $c_{i\downarrow} = h_i^\dagger S_i^+ = h_i^\dagger a_i$. Ignoring higher-order interactions, we derive the effective Hamiltonian with two terms: the kinetic energy term

$$H_{h0} = - \sum_{\mathbf{k}} \omega_0^h(\mathbf{k}) h_{\mathbf{k}} h_{\mathbf{k}}^\dagger \quad (3)$$

with dispersion relation $\omega_0^h(\mathbf{k}) = \frac{\nu t}{2} (\gamma_{\mathbf{k}+\frac{\mathbf{Q}}{2}} + \gamma_{\mathbf{k}-\frac{\mathbf{Q}}{2}})$ and the holon-magnon coupling term

$$H_{hb} = - \frac{\nu t}{i\sqrt{N}} \sum_{\mathbf{k}, \mathbf{q}} h_{\mathbf{k}} h_{\mathbf{k}-\mathbf{q}}^\dagger (M_{\mathbf{k}} a_{\mathbf{q}}^\dagger - M_{\mathbf{k}-\mathbf{q}} a_{-\mathbf{q}}) \quad (4)$$

with $M_{\mathbf{k}} = \gamma_{\mathbf{k}+\frac{\mathbf{Q}}{2}} - \gamma_{\mathbf{k}-\frac{\mathbf{Q}}{2}}$, which describes the motion of the charge in the process of absorbing or emitting magnons. We remark that the kinetic energy term of the magnetic polarons is absent in the square-lattice case [7, 8]. To obtain the single-particle Green's function $G^h(\mathbf{k}, \omega) \equiv \langle \Psi_0 | h_{\mathbf{k}} \frac{1}{\omega - H} h_{\mathbf{k}}^\dagger | \Psi_0 \rangle$, we adopt the SCBA, i.e., considering the rainbow Feynman diagrams sketched in Fig. 1(d), to get the self energy

$$\Sigma^h(\mathbf{k}, \omega) = \sum_{\mathbf{q}} \frac{f(\mathbf{k}, \mathbf{q})}{\omega - \omega_0^h(\mathbf{k} - \mathbf{q}) - \omega_{\mathbf{q}}^s - \Sigma^h(\mathbf{k} - \mathbf{q}, \omega - \omega_{\mathbf{q}}^s)},$$

where a vertex coupling $f(\mathbf{k}, \mathbf{q}) = (\nu t)^2 |M_{\mathbf{k}} v_{\mathbf{q}} - M_{\mathbf{k}-\mathbf{q}} u_{\mathbf{q}}|^2 / N$ originates from holon-magnon interaction.

IV. PHOTOEMISSION AND TUNNELING SPECTROSCOPES

To directly compare with the experiments, we compute the Green's function $G^e(\mathbf{k}, \omega)$ with a relation to $G^h(\mathbf{k}, \omega)$ via

$$G^e(\mathbf{k}, \omega) = -\frac{1}{4} G^h(\mathbf{k} + \frac{\mathbf{Q}}{2}, \omega) - \frac{1}{4} G^h(\mathbf{k} - \frac{\mathbf{Q}}{2}, \omega). \quad (5)$$

The momentum shift $\pm \mathbf{Q}/2$ is induced by the rotation on $|\Psi_0\rangle$, and for triangular Mott antiferromagnets, $\mathbf{Q} = \mathbf{K}$.

We will show the spectral function $A^e(\mathbf{k}, \omega)$ [see Figs. 2(a-b)] and the density of states $D(\omega)$ [see Figs. 2(c-d)], both of which are experimentally detectable through the ARPES [36, 37] and scanning tunneling microscope (STM). The spectral functions $A^e(\mathbf{k}, \omega) \equiv \frac{1}{\pi} \text{Im} G^e(\mathbf{k}, \omega + i\delta)$ are presented in Figs. 2(a-b) for $t/J = \pm 5$ on a $N = 6 \times 6$ lattice with energy resolution $\Delta\omega$. We have confirmed their robustness on

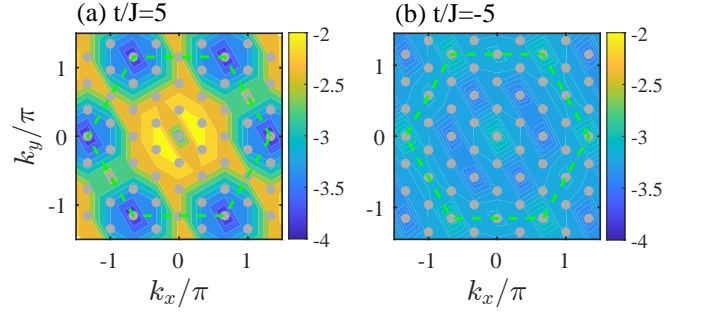


Fig. 3. (Color online.) Energy dispersion. Energy dispersion for a single charge in (a) $t/J = 5$ and (b) $t/J = -5$ from SCBA. The gray dots mark the accessible Bloch momenta on a $N = 6 \times 6$ lattice.

the larger size with the convergence guaranteed by energy resolution $\Delta\omega = 0.01$ (see Appendix). For $t/J = 5$, as shown in Fig. 2(a), we find that, in the spectral function, the sharp peak at momentum $\mathbf{K} = (\frac{4\pi}{3}, 0)$ with the lowest energy signals a well-defined quasiparticle, which separates from the peaks at other momenta with higher energy. Interestingly, unlike the square-lattice case, where the 180° Néel order and the doped hole locate at momenta (π, π) and $(\pi/2, \pi/2)$, respectively, here the momentum of the doped charge is the same as that of the spin background with 120° Néel order. However, for $t/J = -5$, although we can still identify a well-defined quasiparticle peak at momentum $(\frac{2\pi}{3}, 0)$, there are numerous excitations with a fairly close energy scale, as demonstrated in Fig. 2(b), suggesting a heavily reduced bandwidth compared with the $t/J = 5$ side. This observation demonstrates that the doped charge is highly renormalized with much larger effective mass and much smaller quasiparticle weight. The spectral function for $t/J > 0$ and $t/J < 0$ manifests the asymmetric photoemission spectroscopies. Notably, we can observe some Lorentz-like broadening peaks at much higher energies with momenta $(\frac{4\pi}{3}, 0)$ and $(0, 0)$, which reflects the spin dynamics and confirms our theoretical setup.

Moreover, we compute the density of states $D(\omega) = \sum_{\mathbf{k}} A^e(\mathbf{k}, \omega)$ that can be directly probed by STM. As shown in Fig. 2(c), $D(\omega)$ is also asymmetric with respect to $t/J > 0$ and $t/J < 0$. We find $D(\omega)$ characterizes a well-defined quasiparticle when $t/J > 0$, however, for $t/J < 0$, the divergence of $D(\omega)$ near the ground state signals the Van Hove singularity behavior or the nearly flat band [see Fig. 2(d)], suggesting the numerous excitations near the ground state, consistent with many low-energy peaks in a narrow energy window in the spectral functions $A^e(\mathbf{k}, \omega)$ [see Fig. 2(b)].

We remark that the asymmetric spectral functions $A^e(\mathbf{k}, \omega)$ and density of states $D(\omega)$ with respect to $t/J > 0$ and $t/J < 0$ indicate the distinct bandwidth for the doped charge, which can be inferred from the gaps between peaks in $A^e(\mathbf{k}, \omega)$ [see Figs. 2(a) and (b)], or more clearly, from the energy dispersion $\omega^h(\mathbf{k})$ shown in Fig. 3. Within the same color scale, we can find the nearly flat band with vanishingly small bandwidth when $t/J < 0$, but a well-defined dispersive quasiparticle when $t/J > 0$. Further, consistency is shown at a larger lattice

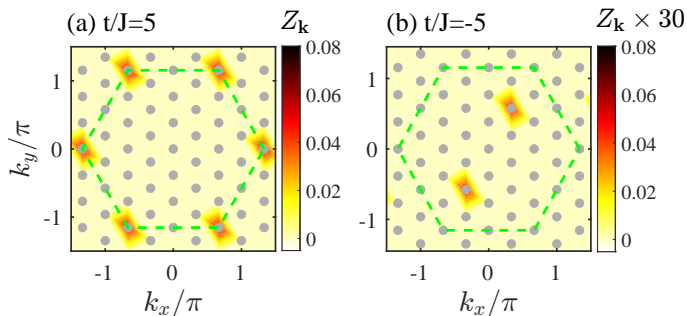


Fig. 4. (Color online). The quasiparticle spectral weight $Z_{\mathbf{k}}$ calculated by DMRG for (a) $t/J = 5$ and (b) $t/J = -5$ with a single charge doping. The gray dots represent the accessible momenta with $N = 6 \times 6$ cylinder geometry.

size (see Appendix). The nearly flat band implies the doped charge is heavily renormalized, giving rise to much larger effective mass or much smaller quasiparticle weight. The minimum in the energy dispersion $\omega^h(\mathbf{k})$ characterizes the ground-state momentum of the doped charge, which is also confirmed by the DMRG simulations below.

V. NUMERICAL SIMULATION

Below we employ DMRG to confirm the validity of SCBA by examining the quasiparticle weight. In addition to the single charge doping, we further examine the finite doping to understand the asymmetric behavior by probing the spin background against doping and further reveal that our proposal works at light doping. Numerically it requires the integral multiple of 3 for system length L_x and width L_y in order to accommodate the 120° Néel order, and DMRG computational cost increases exponentially with L_y , we therefore primarily focus on $L_y = 6$ cylinders with the bond dimension up to $D=20000$. The charge doping can be accurately controlled by implementing U(1) symmetries.

We compute the quasiparticle spectral weight distribution $Z_{\mathbf{k}}$, which is defined by the overlap between the one-charge doped ground-state wave function $\Psi_{1\text{-charge}}$ and the wave function obtained by removing a charge from the half-filled ground state $\Psi_{0\text{-charge}}$, i.e.,

$$Z_{\mathbf{k}} \equiv |\langle \Psi_{1\text{-charge}} | c_{\mathbf{k}} | \Psi_{0\text{-charge}} \rangle|^2. \quad (6)$$

Figures 4(a) and (b) show the contour plot of $Z_{\mathbf{k}}$ for $t/J = 5$ and $t/J = -5$ on $L_y = 6$ cylinders, respectively. The finite $Z_{\mathbf{k}}$ for both $t/J > 0$ and $t/J < 0$ suggest well-defined quasiparticles, consistent with the nature of magnetic polarons. The location of the peaks in $Z_{\mathbf{k}}$ characterizes the ground-state momentum of the doped charge. For $t/J = 5$, the significant peaks locate at momenta \mathbf{K} [see Fig. 4(a)], while for $t/J = -5$, we find that the peaks locate at momentum $\mathbf{K}/2$ [see Fig. 4(b)]. Notably, $Z_{\mathbf{k}}$ at $t/J = -5$ is highly suppressed, thus we multiply it with a factor 30 to clearly compare the

two sides. The finite $Z_{\mathbf{k}}$ and the ground-state momenta obtained from DMRG confirm the SCBA results, demonstrating the magnetic polaron theory indeed captures the nature of a doped charge. The distinct momenta for opposite signs of t/J also manifest the particle-hole asymmetry. Given the relation $Z_{\mathbf{k}} \sim m/m^*$, with m the bare electron mass and m^* the effective mass of quasiparticle, our results indicate that the effective mass of the doped single charge at $t/J < 0$ is much larger than $t/J > 0$, or equivalently, the band at $t/J < 0$ is quite narrow or nearly flat.

To explore the distinct behavior of the doped charges at two sides and check the validity of our magnetic polaron theory, we probe the spin channel by computing the static spin structure factor

$$S(\mathbf{k}) = \frac{1}{N} \sum_{i,j} \langle \mathbf{S}_i \cdot \mathbf{S}_j \rangle e^{i\mathbf{k} \cdot (\mathbf{r}_i - \mathbf{r}_j)}, \quad (7)$$

which also can be directly probed in an optical lattice [33]. At half filling, the 120° Néel order is characterized by the sharp peaks of $S(\mathbf{k})$ at $\mathbf{k} = \mathbf{Q}$ [see Fig. 1(c)]. To probe the evolution of the spin background with doping, we keep track of $S(\mathbf{k} = \mathbf{Q})$ as a function of doping concentration δ , as shown in Figs. 5. For $t/J > 0$, we find the spin background is insensitive to the light doping, as indicated by the robust sharp peak of $S(\mathbf{k} = \mathbf{Q})$ for $\delta \lesssim 10\%$ [see Fig. 5 (a)]. However, the 120° Néel order is rapidly weakened at $t/J < 0$ even with a much lower doping level $\delta \lesssim 5\%$ [see Fig. 5 (b)], suggesting the motion of the charge may induce a global distortion on the spin background, which in turn would further dress the doped charge, leading to the significantly enhanced effective mass. The 120° Néel order is also the precondition of magnetic polaron theory, and our findings of $S(\mathbf{k})$ against doping suggest such a theory is valid at least for $\delta \lesssim 5\%$ at both sides, while for a wider range at the $t/J > 0$ side. The distinct nature of the ground state in both charge and spin channels exhibits the particle-hole asymmetry and reveals the intricate interplay between the charge and spin degrees of freedom.

VI. SUMMARY AND OUTLOOK

In summary, we theoretically predict asymmetric photoemission and tunneling spectroscopies for the lightly doped triangular Mott antiferromagnets and identify two distinct types of magnetic polarons on frustrated lattices: the lightly renormalized quasiparticle with the same momentum as the spin background, and the heavily renormalized quasiparticle with a shifted momentum, which resolves discrepancies in previous works [47–50]. The latter provides a new way to engineer the flat bands and explore the possible topology and Kondo physics in doped Mott insulators. We further show the asymmetric responses of the spin background against doping and confirm the validity of our theory at least within $\delta \lesssim 5\%$. Our findings might motivate future theoretical studies on the interplay between the local degrees of freedom and the geometric frustration, or on the possible emerged phases with further increased doping concentration [61], both of which

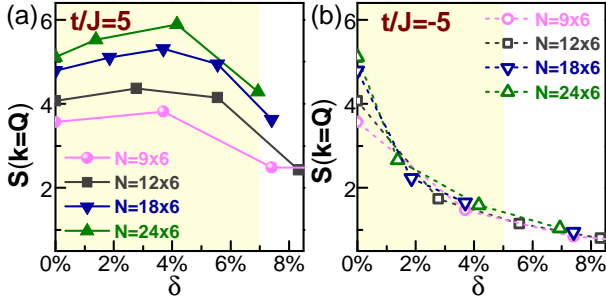


Fig. 5. (Color online). The spin structure factor $S(\mathbf{k} = \mathbf{Q})$ as a function of charge doping concentration δ for $t/J = 5$ (a) and $t/J = -5$ (b) on $L_y = 6$ cylinders. Results are from DMRG calculations.

are of fundamental importance for understanding the Fermi-Hubbard physics on frustrated lattices.

Moreover, the triangular-lattice Fermi-Hubbard model has recently been realized on the frustrated optical lattices [24], in which both the ratio U/t and charge doping can be accurately tuned [18–31, 38, 41], then our predictions of the spectral function and the static spin structure factor are readily verified based on recently developed techniques including ARPES [36, 37] and the coherent manipulation of spin correlations [33]. Additionally, our prediction of the spectral function and the density of states at light doping can also be directly tested in the TMD and its heterostructures by the STM and nano-ARPES techniques [39, 40, 46]. These proposals based on our theory may also inspire more experimental ideas beyond the extensively studied square-lattice case.

ACKNOWLEDGMENTS

We would like to thank Z. Y. Weng, F. C. Zhang, T. K. Ng, A. Vishwanath, D. N. Sheng, J. X. Li, T. Li, J. H. Mao, Y. Xu, M. Knap for helpful discussions. This work was supported by the National Natural Science Foundation of China (Grant No. 12074375), the Innovation Program for Quantum Science and Technology (Grant No. 2-6), the Fundamental Research Funds for the Central Universities, the Strategic Priority Research Program of CAS (Grant No. XDB33000000) and the start-up funding of KITS at UCAS.

Appendix A: Particle-hole transformations

For the t - J model [see Eq. (2)] in the main text, the Hilbert space subject to the single-occupation condition and the single charge doping is realized by removing a fermion from the half-filled background, i.e., $\sum_i n_i = N - 1$. We refer to the electron-doped and hole-doped physics as the cases of $t/J > 0$ and $t/J < 0$, due to the particle-hole asymmetry. Here we give a more detailed explanation for it.

At half-filling $\sum_i n_i = N$, the Hubbard model in the large U limit can be reduced to a pure Heisenberg model, which harbors the 120° Néel order. For a single hole doping, i.e.,

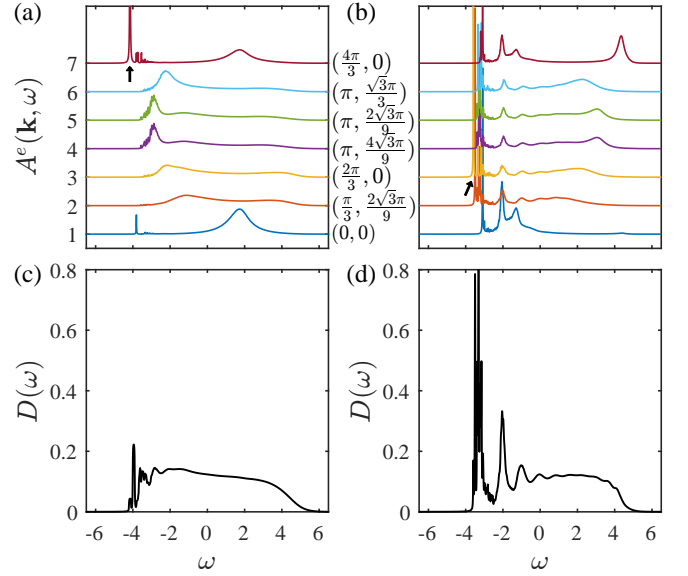


FIG. 6. (Color online) Spectra and density of states from the SCBA at 12×12 lattice size. A well-defined quasiparticle peak (marked by black arrows) lies at the bottom of spectrum with $\mathbf{K} = (\frac{4\pi}{3}, 0)$ for $t/J = 5$ in (a) and $(\frac{2\pi}{3}, 0)$ for $t/J = -5$ in (b), respectively. The density of states $D(\omega)$ features a vanishing gap in a continuum limit for $t/J = 5$ in (c) and $t/J = -5$ in (d). Here we set $|t| = 1$ as the unity of energy and energy resolution $\Delta\omega = 0.01$.

$\sum_i n_i = N - 1$, the low energy for the Hubbard model in Eq. (1) in the main text can be well captured by the t - J model with Hilbert space subject to the single-occupation condition. Similarly, for a single electron doping, i.e., $\sum_i n_i = N + 1$, the perturbation mechanism will give the following low energy Hamiltonian,

$$H = -t \sum_{\langle ij \rangle \sigma} \tilde{\mathcal{P}}(c_{i\sigma}^\dagger c_{j\sigma} + c_{j\sigma}^\dagger c_{i\sigma}) \tilde{\mathcal{P}} + J \sum_{\langle ij \rangle} \mathbf{S}_i \cdot \mathbf{S}_j, \quad (\text{A1})$$

where instead, the projector $\tilde{\mathcal{P}}$ removes empty occupancy. Subsequently, we introduce the particle-hole transformation

$$c_{i\sigma} \rightarrow c_{i\sigma}^\dagger, c_{i\sigma}^\dagger \rightarrow c_{i\sigma}, \quad (\text{A2})$$

which changes the sign of the hopping integral in Eq. (A1), i.e., $t \rightarrow -t$, but keeps J invariant. Significantly, the particle number is mapped to

$$\sum_i n_i = N + 1 \rightarrow \sum_i n_i = N - 1. \quad (\text{A3})$$

In this sense, different signs of the hopping integral t refer to the electron-doped or hole-doped case for the t - J model in Eq. (2) in the main text.

Appendix B: Finite Size effect

Here we present the results from the self-consistent Born approximation (SCBA) with a larger lattice size. Figure 6 depicts the results calculated by SCBA with 12×12 lattice size, where the spectrum and densities of states are consistent with the 6×6 lattice. Furthermore, some noise like subtle structure gets suppressed. In Fig. 6(d), the extremely sharp peak indicates the Van Hove singularity behavior. In Fig. 7, we plot the dispersion relations for $t/J = 5$ in the left panel and $t/J = -5$ in the right panel. Figure 7(b) for $t/J = -5$ shows a much narrower bandwidth, implied by the almost invariant color distribution with the same color scale as that of the $t/J = 5$ side in Fig. 7(a).

Appendix C: The momentum distribution at light doping

In this section, we examine the momentum distribution of the doped charge at light doping. The momentum distribution of the doped charge can be calculated by

$$n_{\mathbf{k}}^c \equiv 1 - \sum_{\sigma} \left\langle \Psi_G \left| c_{\mathbf{k}\sigma}^{\dagger} c_{\mathbf{k}\sigma} \right| \Psi_G \right\rangle, \quad (\text{C1})$$

where $|\psi_G\rangle$ is the ground state, and $c_{\mathbf{k}\sigma}^{\dagger}$ ($c_{\mathbf{k}\sigma}$) is the fermion creation (annihilation) operators with momentum \mathbf{k} and spin $\sigma = \uparrow, \downarrow$. The factor 1 corresponds to the momentum distribution at half filling for a Mott insulator.

In Fig. 8, we show the momentum distribution of the doped charge $n_{\mathbf{k}}^c$ at finite doping on lattices with two different sizes $N = 9 \times 6$ and $N = 18 \times 6$. We find the physical indications are robust against system size. As shown in Figure 8(a) or (b) for $t/J = 5$, we find that, with the increase of the doping concentration, the Fermi pockets are gradually formed around \mathbf{K} points compared with the single charge momentum \mathbf{K} [see Fig. 2(a) and Fig. 3(a) in the main text]. In particular, since the momentum is a discrete value $(2\pi/L_i) \cdot m_i$ in the direction i , where $m_i \in \mathbb{Z}$ and $i = x, y$ with the finite system size L_x and L_y , the value of the Fermi momentum is a size-dependent quantity. However, the numerical observations of

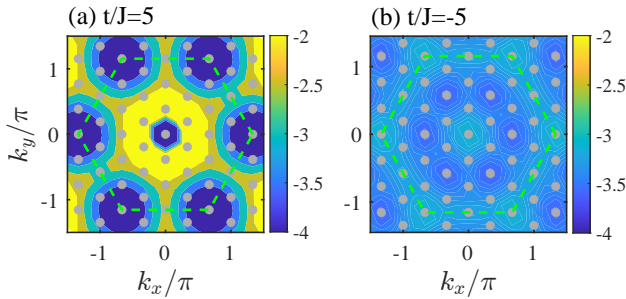


FIG. 7. (Color online) Dispersion for (a) $t/J = 5$ and (b) $t/J = -5$. We can clearly see that the bandwidth for $t/J = 5$ is much larger than that of $t/J = -5$. Here we set $|t| = 1$ as the unity of energy and energy resolution $\Delta\omega = 0.01$.

the formation of Fermi pockets around \mathbf{K} are consistent with such quasiparticle behavior. By contrast, for the other side $t/J = -5$, as shown in Fig. 8(c,d), the doped charge forms a large Fermi surface with a wider distribution of the Fermi momentum, as indicated by the sudden drop of $n_{\mathbf{k}}^c$. The large Fermi surface suggests that many low-energy quasiparticles with different momenta share close energies, which is consistent with filling the nearly flat band that emerges for the single-charge doping case at $t/J < 0$, as shown in Fig. 2(b) and Fig. 3(b) in the main text.

We further confirm the above interpretations by slightly increase the doping concentrations from $\delta = 1/27$ [see Fig. 8] to $\delta = 1/24$ [see Fig. 9], and find the numerical observations are consistent with the physical picture mentioned above.

Appendix D: Details for the SCBA calculations

At half-filling, the strong Hubbard interaction penalizes double occupancy at sites and thus the ground state harbors well-established 120° antiferromagnetic collinear order that is described by a pure Heisenberg model $H_J = J \sum_{\langle ij \rangle} \mathbf{S}_i \cdot \mathbf{S}_j$.

We can apply the spin wave theory to characterize the low energy excitations. Without loss of generality, we set the AFM order residing the XZ-plane by rotating each spin by an angle $\mathbf{Q} \cdot \mathbf{r}_i$ along y-axis at site i

$$H_J \rightarrow -\frac{J}{2} \sum_{\langle ij \rangle} S_i^z S_j^z + J \sum_{\langle ij \rangle} \left(\frac{1}{2} S_i^x S_j^x + S_i^y S_j^y \right) + \sin \mathbf{Q} \cdot \mathbf{r}_{ij} (S_i^x S_j^z - S_i^z S_j^x), \quad (\text{D1})$$

where $\mathbf{r}_{ij} \equiv \mathbf{r}_i - \mathbf{r}_j$ and \mathbf{Q} is the momentum of spin order. The second term in Eq. (D1) is from geometric frustrations, with no counterpart in a square lattice. The magnon polarons can be described by the HP bosons (in the large S limit)

$$S_i^z = S - a_i^\dagger a_i, S_i^+ = a_i, S_i^- = a_i^\dagger, \quad (\text{D2})$$

Here $S_i^\pm = S^x \pm iS^y$ is the spin ladder operators. To the leading order, Eq. (D2) yields an effective Hamiltonian for magnons,

$$H_a = \frac{J}{2} \sum_i 2S\nu n_i + \frac{SJ}{4} \left(-3a_i a_j + a_i a_j^\dagger + a_i^\dagger a_j - 3a_i^\dagger a_j^\dagger \right). \quad (\text{D3})$$

The last term in Eq. (D1) involves higher-order magnon interactions and can be safely neglected. We can diagonalize $H_a = \sum_{\mathbf{k}} \frac{\nu}{2} JS\omega_{\mathbf{k}}^s \beta_{\mathbf{k}}^\dagger \beta_{\mathbf{k}}$ in Eq. (D3) by the Bogoliubov transformation

$$\beta_{\mathbf{k}} = u_{\mathbf{k}} a_{\mathbf{k}} - v_{\mathbf{k}} a_{-\mathbf{k}}^\dagger, \quad (\text{D4})$$

$$\beta_{-\mathbf{k}}^\dagger = -v_{\mathbf{k}} a_{\mathbf{k}} + u_{\mathbf{k}} a_{-\mathbf{k}}^\dagger, \quad (\text{D5})$$

where $\gamma_{\mathbf{k}} = \frac{1}{\nu} \sum_{\delta} e^{i\mathbf{k} \cdot \delta}$ sums over all $\nu = 6$ nearest-neighbor sites. Here $\omega_{\mathbf{k}}^a = \sqrt{(1 - \gamma_{\mathbf{k}})(1 + 2\gamma_{\mathbf{k}})}$ and $\omega_{\mathbf{k}}^s = \frac{\nu}{2} JS\omega_{\mathbf{k}}^a$ is the magnon's dispersion. The coefficients $u_{\mathbf{k}}$ and $v_{\mathbf{k}}$ are the

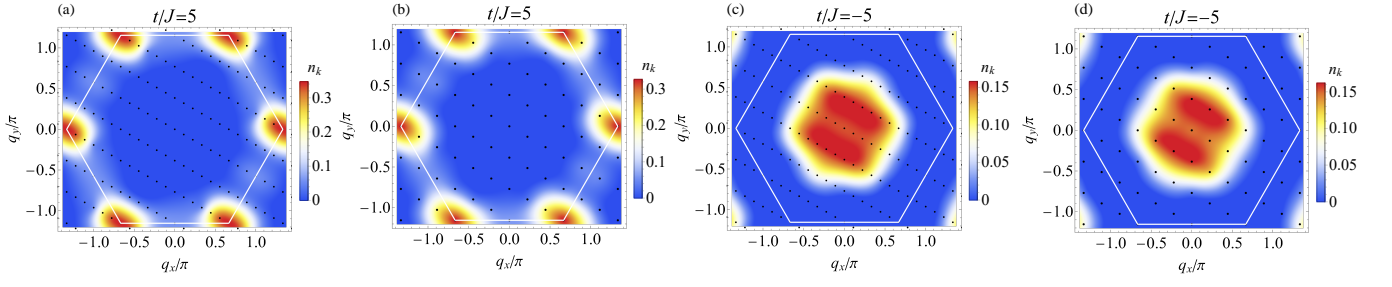


FIG. 8. (Color online) The momentum distribution of the doped charge $n_{\mathbf{k}}^c$ with doping concentration $\delta = 1/27$. $t/J = 5$ for (a,b) and $t/J = -5$ for (c,d), while $N = 18 \times 6$ for (a,c) and $N = 9 \times 6$ for (b,d). The black dots represent the accessible momenta in the Brillouin zone (white lines). Interpolation has been applied.

usual Bogoliubov factors in the linear spin-wave theory

$$u_{\mathbf{k}} = \sqrt{\frac{1 + \gamma_{\mathbf{k}}/2 + \omega_{\mathbf{k}}^a}{2\omega_{\mathbf{k}}^a}}, \quad v_{\mathbf{k}} = \text{sign}(\gamma_{\mathbf{k}}) \sqrt{\frac{1 + \gamma_{\mathbf{k}}/2 - \omega_{\mathbf{k}}^a}{2\omega_{\mathbf{k}}^a}}. \quad (\text{D6})$$

The half-filled ground state after rotation accordingly can assume the form as

$$|\Psi_0\rangle = \exp\left(-\sum_{\mathbf{k}} \frac{v_{\mathbf{k}}}{u_{\mathbf{k}}} a_{\mathbf{k}} a_{-\mathbf{k}}\right) |\text{Néel}\rangle, \quad (\text{D7})$$

with $|\text{Néel}\rangle$ being a classical 120° AFM order. The SCBA method considers the propagation of a holon excitation by absorbing or emitting magnons a_i on a quantum Néel ground state in Eq. (D7). On the rotated state $|\Psi_0\rangle$, we assume a spinless holon h_i^\dagger is to be created by removing a spin- \uparrow electron. Namely, we have a typical fractionalization scheme,

$$c_{i\uparrow} = h_i^\dagger, c_{i\downarrow} = h_i^\dagger S_i^+ = h_i^\dagger a_i, \quad (\text{D8})$$

By ignoring higher-order interactions involving multi-magnons, the hopping terms will split into two terms: the kinetic energy term for the holon,

$$H_{h0} = -\sum_{\mathbf{k}} \omega_0^h(\mathbf{k}) h_{\mathbf{k}} h_{\mathbf{k}}^\dagger, \quad (\text{D9})$$

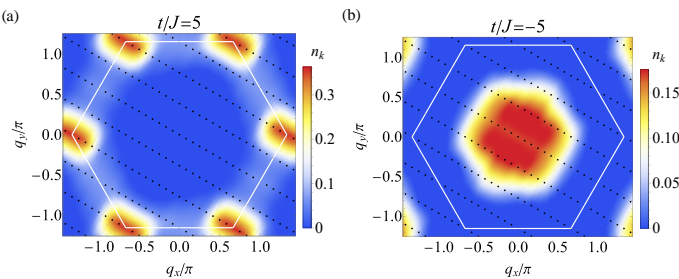


FIG. 9. (Color online) The momentum distribution of the doped charge $n_{\mathbf{k}}^c$ with doping concentration $\delta = 1/24$. $t/J = 5$ for (a) and $t/J = -5$ for (b) on $N = 24 \times 6$ lattice. The black dots represent the accessible momenta in the Brillouin zone (white lines). Interpolation has been applied.

with a bare dispersion $\omega_0^h(\mathbf{k}) = \frac{\nu t}{2} (\gamma_{\mathbf{k}+\mathbf{Q}/2} + \gamma_{\mathbf{k}-\mathbf{Q}/2})$ and the holon-magnon coupling terms

$$H_{hb} = -\frac{\nu t}{i\sqrt{N}} \sum_{\mathbf{k}} h_{\mathbf{k}} h_{\mathbf{k}-\mathbf{q}}^\dagger (M_{\mathbf{k}} a_{\mathbf{q}}^\dagger - M_{\mathbf{k}-\mathbf{q}} a_{-\mathbf{q}}), \quad (\text{D10})$$

with $M_{\mathbf{k}} = \gamma_{\mathbf{k}+\mathbf{Q}/2} - \gamma_{\mathbf{k}-\mathbf{Q}/2}$. The existence of the kinetic term H_{h0} in Eq. (D9), which is absent in the square lattice, indicates the Trugman loop may not play a leading role, in contrast to the square lattice. The holon-magnon interaction H_{hb} opens a channel for propagation of a doped charge by absorbing or emitting magnons. The holon's Green's function with a definition $G^h(\mathbf{k}, \omega) = \langle \Psi_0 | h_{\mathbf{k}} \frac{1}{\omega - H} h_{\mathbf{k}}^\dagger | \Psi_0 \rangle$, will be determined a self-consistent equation by only involving non-crossed Feynman diagrams for the holon's self energy $\Sigma^h(\mathbf{k}, \omega)$,

$$\Sigma^h(\mathbf{k}, \omega) = \sum_{\mathbf{q}} \frac{f(\mathbf{k}, \mathbf{q})}{\omega - \omega_0^h(\mathbf{k} - \mathbf{q}) - \omega_{\mathbf{q}}^s - \Sigma^h(\mathbf{k} - \mathbf{q}, \omega - \omega_{\mathbf{q}}^s)}, \quad (\text{D11})$$

with a vertex coupling,

$$f(\mathbf{k}, \mathbf{q}) = \frac{1}{N} (\nu t)^2 |M_{\mathbf{k}} v_{\mathbf{q}} - M_{\mathbf{k}-\mathbf{q}} u_{\mathbf{q}}|^2. \quad (\text{D12})$$

The experimentally detectable electron's Green's function $G^e(\mathbf{k}, \omega)$ is related based the fractionalization scheme in Eq. (D8),

$$G^e(\mathbf{k}, \omega) = -\frac{1}{4} G^h(\mathbf{k} + \frac{\mathbf{Q}}{2}, \omega) - \frac{1}{4} G^h(\mathbf{k} - \frac{\mathbf{Q}}{2}, \omega), \quad (\text{D13})$$

where $\mathbf{Q}/2$ arises from the rotating operations on the spins at each site. The self-consistent equation for the self-energy Σ^h can be tackled by numerical iterations on randomly initialized values of $\Sigma^h(\mathbf{k}, \omega)$. At the side of $t < 0$, one needs a large number of iterations to reach the convergence, which may be traced back to the existence of the nearly flat band and the extremely weak quasiparticle weight.

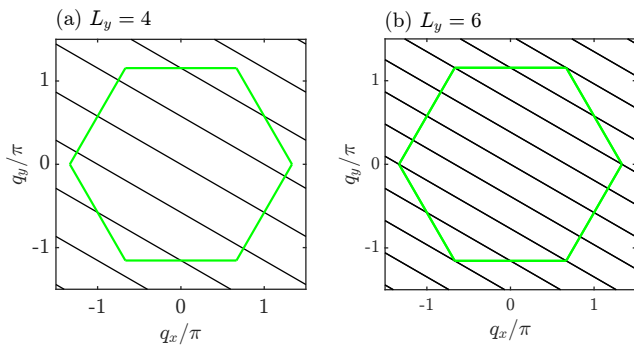


FIG. 10. Finite size effects for accessible momenta marked by black lines in the Brillouin zone: (a) four-leg and (b) six-leg ladders. The boundary of the first Brillouin zone is guided by a green hexagon.

Appendix E: Comparison with previous works

The fate of the injected charges in the Fermi-Hubbard model on a triangular lattice is a long-standing issue but with controversial conclusions. In previous literature, no consistent results are reached, even for those using the same SCBA method and exact diagonalization method. Here we give a

detailed illustration.

Ref. [47] studied the single-charge problem on a triangular lattice. Its predictions on the ground state momenta are peaked at \mathbf{K} and $\mathbf{K}/2$ respectively for $t/J = \pm 5$, which is consistent with ED on a comparatively small lattice. However, controversies were erupted against this prediction with ED on a larger lattice in Ref. [62]. Ref. [62] revisited the problem with the same SCBA method, but affirms the absence of quasiparticle excitations outside the neighborhood of magnetic Goldstone modes at the side $t/J = 5$, the ground state momentum resides \mathbf{K} for $t/J = 5$ and Γ for $t/J < -5$ [62], which is consistent with ED on a larger lattice. Concomitantly, other methods report discrepancies. For example, Ref. [63] adopted a cumulant version of Mori-Zwanzig projection techniques to deal with spin bag quasiparticle or magnetic polaron, and found the ground-state momenta locates in \mathbf{K} points at both sides $t > 0$ and $t < 0$. The discrepancies motivate our works, in particular by applying the advanced DMRG method to avoid the severe finite size effect in ED. For example, at 6×4 lattice size, both \mathbf{K} and $\mathbf{K}/2$ are not accessible (see 10(a)) and on the width-three ladder, the spin background has a finite gap due to the spontaneous dimerization. The minimum lattice size to capture the 120° order in the absence of dimerization is 6×6 (see 10(b)), which is beyond the capacity of ED.

-
- [1] P. A. Lee, N. Nagaosa, and X.-G. Wen, Doping a Mott insulator: Physics of high-temperature superconductivity, *Rev. Mod. Phys.* **78**, 17 (2006).
 - [2] P. W. Anderson, The resonating valence bond state in La_2CuO_4 and superconductivity, *Science* **235**, 1196 (1987).
 - [3] B. Keimer, S. A. Kivelson, M. R. Norman, S. Uchida, and J. Zaanen, From quantum matter to high-temperature superconductivity in copper oxides, *Nature* **518**, 179 (2015).
 - [4] E. Dagotto, Correlated electrons in high-temperature superconductors, *Rev. Mod. Phys.* **66**, 763 (1994).
 - [5] W. F. Brinkman and T. M. Rice, Single-particle excitations in magnetic insulators, *Phys. Rev. B* **2**, 1324 (1970).
 - [6] B. I. Shraiman and E. D. Siggia, Mobile vacancies in a quantum heisenberg antiferromagnet, *Phys. Rev. Lett.* **61**, 467 (1988).
 - [7] C. L. Kane, P. A. Lee, and N. Read, Motion of a single hole in a quantum antiferromagnet, *Phys. Rev. B* **39**, 6880 (1989).
 - [8] G. Martinez and P. Horsch, Spin polarons in the t - J model, *Phys. Rev. B* **44**, 317 (1991).
 - [9] Z. Zhu, H.-C. Jiang, Y. Qi, C. Tian, and Z.-Y. Weng, Strong correlation induced charge localization in antiferromagnets, *Scientific reports* **3**, 1 (2013).
 - [10] Z. Zhu and Z.-Y. Weng, Quasiparticle collapsing in an anisotropic t - J ladder, *Phys. Rev. B* **92**, 235156 (2015), [arXiv:1409.3241 \[cond-mat.str-el\]](https://arxiv.org/abs/1409.3241).
 - [11] Z. Zhu, Q.-R. Wang, D. N. Sheng, and Z.-Y. Weng, Exact sign structure of the t - J chain and the single hole ground state, *Nuclear Physics B* **903**, 51 (2016), [arXiv:1510.07634 \[cond-mat.str-el\]](https://arxiv.org/abs/1510.07634).
 - [12] Z. Zhu, D. N. Sheng, and Z.-Y. Weng, Intrinsic translational symmetry breaking in a doped mott insulator, *Phys. Rev. B* **98**, 035129 (2018).
 - [13] S. Chen, Q.-R. Wang, Y. Qi, D. N. Sheng, and Z.-Y. Weng, Single-hole wave function in two dimensions: A case study of the doped Mott insulator, *Phys. Rev. B* **99**, 205128 (2019).
 - [14] S. Chen, Z. Zhu, and Z.-Y. Weng, Two-hole ground state wavefunction: Non-bcs pairing in a t - j two-leg ladder, *Phys. Rev. B* **98**, 245138 (2018).
 - [15] J.-Y. Zhao, S. A. Chen, H.-K. Zhang, and Z.-Y. Weng, Two-hole ground state: Dichotomy in pairing symmetry, [arXiv preprint arXiv:2106.14898](https://arxiv.org/abs/2106.14898) (2021).
 - [16] A. Bohrdt, E. Demler, F. Pollmann, M. Knap, and F. Grusdt, Parton theory of angle-resolved photoemission spectroscopy spectra in antiferromagnetic Mott insulators, *Phys. Rev. B* **102**, 035139 (2020).
 - [17] A. Bohrdt, E. Demler, and F. Grusdt, Rotational resonances and regge-like trajectories in lightly doped antiferromagnets, *Phys. Rev. Lett.* **127**, 197004 (2021).
 - [18] C. Gross and W. S. Bakr, Quantum gas microscopy for single atom and spin detection, *Nature Physics* (2021).
 - [19] A. Bohrdt, L. Homeier, C. Reinmoser, E. Demler, and F. Grusdt, Exploration of doped quantum magnets with ultracold atoms, *Annals of Physics* **435**, 168651 (2021), special issue on Philip W. Anderson.
 - [20] W. S. Bakr, J. I. Gillen, A. Peng, S. Fölling, and M. Greiner, A quantum gas microscope for detecting single atoms in a Hubbard-regime optical lattice, *Nature* **462**, 74 (2009).
 - [21] M. F. Parsons, A. Mazurenko, C. S. Chiu, G. Ji, D. Greif, and M. Greiner, Site-resolved measurement of the spin-correlation function in the Fermi-Hubbard model, *Science* **353**, 1253 (2016).
 - [22] J. F. Sherson, C. Weitenberg, M. Endres, M. Cheneau, I. Bloch, and S. Kuhr, Single-atom-resolved fluorescence imaging of an atomic Mott insulator, *Nature* **467**, 68 (2010).
 - [23] L. W. Cheuk, M. A. Nichols, K. R. Lawrence, M. Okan,

- H. Zhang, E. Khatami, N. Trivedi, T. Paiva, M. Rigol, and M. W. Zwierlein, Observation of spatial charge and spin correlations in the 2D Fermi-Hubbard model, *Science* **353**, 1260 (2016).
- [24] J. Yang, L. Liu, J. Mongkolkeha, and P. Schauss, Site-resolved imaging of ultracold fermions in a triangular-lattice quantum gas microscope, *PRX Quantum* **2**, 020344 (2021).
- [25] F. Schäfer, T. Fukuhara, S. Sugawa, Y. Takasu, and Y. Takahashi, Tools for quantum simulation with ultracold atoms in optical lattices, *Nature Reviews Physics* **2**, 411 (2020).
- [26] M. Boll, T. A. Hilker, G. Salomon, A. Omran, J. Nespolo, L. Pollet, I. Bloch, and C. Gross, Spin- and density-resolved microscopy of antiferromagnetic correlations in Fermi-Hubbard chains, *Science* **353**, 1257 (2016).
- [27] P. T. Brown, D. Mitra, E. Guardado-Sanchez, P. Schauß, S. S. Kondov, E. Khatami, T. Paiva, N. Trivedi, D. A. Huse, and W. S. Bakr, Spin-imbalance in a 2D Fermi-Hubbard system, *Science* **357**, 1385 (2017).
- [28] P. T. Brown, D. Mitra, E. Guardado-Sanchez, R. Nourafkan, A. Reymbaut, C.-D. Hébert, S. Bergeron, A.-M. S. Tremblay, J. Kokalj, D. A. Huse, P. Schauß, and W. S. Bakr, Bad metallic transport in a cold atom Fermi-Hubbard system, *Science* **363**, 379 (2019).
- [29] E. Guardado-Sanchez, A. Morningstar, B. M. Spar, P. T. Brown, D. A. Huse, and W. S. Bakr, Subdiffusion and heat transport in a tilted two-dimensional Fermi-Hubbard system, *Phys. Rev. X* **10**, 011042 (2020).
- [30] J. Koepsell, S. Hirthe, D. Bourgund, P. Sompet, J. Vijayan, G. Salomon, C. Gross, and I. Bloch, Robust bilayer charge pumping for spin- and density-resolved quantum gas microscopy, *Phys. Rev. Lett.* **125**, 010403 (2020).
- [31] T. Hartke, B. Oreg, N. Jia, and M. Zwierlein, Doublon-hole correlations and fluctuation thermometry in a Fermi-Hubbard gas, *Phys. Rev. Lett.* **125**, 113601 (2020).
- [32] I. Bloch, J. Dalibard, and S. Nascimbene, Quantum simulations with ultracold quantum gases, *Nature Physics* **8**, 267 (2012).
- [33] N. Wurz, C. F. Chan, M. Gall, J. H. Drewes, E. Cocchi, L. A. Miller, D. Pertot, F. Brennecke, and M. Köhl, Coherent manipulation of spin correlations in the Hubbard model, *Phys. Rev. A* **97**, 051602 (2018).
- [34] C. S. Chiu, G. Ji, A. Bohrdt, M. Xu, M. Knap, E. Demler, F. Grusdt, M. Greiner, and D. Greif, String patterns in the doped Hubbard model, *Science* **365**, 251 (2019).
- [35] J. Koepsell, J. Vijayan, P. Sompet, F. Grusdt, T. A. Hilker, E. Demler, G. Salomon, I. Bloch, and C. Gross, Imaging magnetic polarons in the doped Fermi-Hubbard model, *Nature* **572**, 358 (2019).
- [36] P. T. Brown, E. Guardado-Sanchez, B. M. Spar, E. W. Huang, T. P. Devereaux, and W. S. Bakr, Angle-resolved photoemission spectroscopy of a Fermi-Hubbard system, *Nature Physics* **16**, 26 (2020).
- [37] A. Bohrdt, D. Greif, E. Demler, M. Knap, and F. Grusdt, Angle-resolved photoemission spectroscopy with quantum gas microscopes, *Phys. Rev. B* **97**, 125117 (2018).
- [38] M. Lewenstein, A. Sanpera, and V. Ahufinger, *Ultracold Atoms in Optical Lattices: Simulating quantum many-body systems* (Oxford University Press, 2012).
- [39] Y. Tang, L. Li, T. Li, Y. Xu, S. Liu, K. Barmak, K. Watanabe, T. Taniguchi, A. H. MacDonald, J. Shan, *et al.*, Simulation of Hubbard model physics in WSe_2/WS_2 moiré superlattices, *Nature* **579**, 353 (2020).
- [40] D. M. Kennes, M. Claassen, L. Xian, A. Georges, A. J. Millis, J. Hone, C. R. Dean, D. Basov, A. N. Pasupathy, and A. Rubio, Moiré heterostructures as a condensed-matter quantum simulator, *Nature Physics* **17**, 155 (2021).
- [41] C. Chin, R. Grimm, P. Julienne, and E. Tiesinga, Feshbach resonances in ultracold gases, *Rev. Mod. Phys.* **82**, 1225 (2010).
- [42] Y. Pan, S. Fölsch, Y. Nie, D. Waters, Y.-C. Lin, B. Jariwala, K. Zhang, K. Cho, J. A. Robinson, and R. M. Feenstra, Quantum-confined electronic states arising from the moiré pattern of MoS_2 - WSe_2 heterobilayers, *Nano Letters* **18**, 1849 (2018).
- [43] L. Wang, E.-M. Shih, A. Ghiotto, L. Xian, D. A. Rhodes, C. Tan, M. Claassen, D. M. Kennes, Y. Bai, B. Kim, *et al.*, Correlated electronic phases in twisted bilayer transition metal dichalcogenides, *Nature materials* **19**, 861 (2020).
- [44] E. C. Regan, D. Wang, C. Jin, M. I. B. Utama, B. Gao, X. Wei, S. Zhao, W. Zhao, Z. Zhang, K. Yumigeta, *et al.*, Mott and generalized wigner crystal states in WSe_2/WS_2 moiré superlattices, *Nature* **579**, 359 (2020).
- [45] L. An, X. Cai, D. Pei, M. Huang, Z. Wu, Z. Zhou, J. Lin, Z. Ying, Z. Ye, X. Feng, *et al.*, Interaction effects and superconductivity signatures in twisted double-bilayer WSe_2 , *Nanoscale horizons* **5**, 1309 (2020).
- [46] S. Lisi, X. Lu, T. Benschop, T. A. de Jong, P. Stepanov, J. R. Duran, F. Margot, I. Cucchi, E. Cappelli, A. Hunter, *et al.*, Observation of flat bands in twisted bilayer graphene, *Nature Physics* **17**, 189 (2021).
- [47] M. Azzouz and T. Dombre, Motion of holes on the triangular lattice studied using the t-j model, *Phys. Rev. B* **53**, 402 (1996).
- [48] A. E. Trumper, C. J. Gazza, and L. O. Manuel, Quasiparticle vanishing driven by geometrical frustration, *Phys. Rev. B* **69**, 184407 (2004).
- [49] M. Vojta, Spin polarons in triangular antiferromagnets, *Phys. Rev. B* **59**, 6027 (1999).
- [50] P. Srivastava and A. Singh, Hole and electron dynamics in a triangular-lattice antiferromagnet: Interplay of frustration and spin fluctuations, *Phys. Rev. B* **72**, 224409 (2005).
- [51] W. Kadow, L. Vanderstraeten, and M. Knap, Hole Spectral Function of a Chiral Spin Liquid in the Triangular Lattice Hubbard Model, arXiv e-prints, arXiv:2202.03458 (2022), arXiv:2202.03458 [cond-mat.str-el].
- [52] S. Sachdev, Kagomé- and triangular-lattice heisenberg antiferromagnets: Ordering from quantum fluctuations and quantum-disordered ground states with unconfined bosonic spinons, *Phys. Rev. B* **45**, 12377 (1992).
- [53] F. Wang and A. Vishwanath, Spin-liquid states on the triangular and Kagomé lattices: A projective-symmetry-group analysis of schwinger boson states, *Phys. Rev. B* **74**, 174423 (2006).
- [54] A. L. Chernyshev and M. E. Zhitomirsky, Spin waves in a triangular lattice antiferromagnet: Decays, spectrum renormalization, and singularities, *Phys. Rev. B* **79**, 144416 (2009).
- [55] X.-Y. Song, C. Wang, A. Vishwanath, and Y.-C. He, Unifying description of competing orders in two-dimensional quantum magnets, *Nature communications* **10**, 1 (2019).
- [56] Z. Zhu, H.-C. Jiang, D.-N. Sheng, and Z.-Y. Weng, Nature of strong hole pairing in doped Mott antiferromagnets, *Scientific reports* **4**, 1 (2014).
- [57] H.-C. Jiang, S. Chen, and Z.-Y. Weng, Critical role of the sign structure in the doped mott insulator: Luther-emery versus fermi-liquid-like state in quasi-one-dimensional ladders, *Phys. Rev. B* **102**, 104512 (2020).
- [58] Q.-H. Wang, D.-H. Lee, and P. A. Lee, Doped t-J model on a triangular lattice: Possible application to $\text{Na}_x\text{CoO}_2 \cdot y\text{H}_2\text{O}$ and $\text{Na}_{1-x}\text{TiO}_2$, *Phys. Rev. B* **69**, 092504 (2004).
- [59] S. R. White, Density matrix formulation for quantum renormalization groups, *Phys. Rev. Lett.* **69**, 2863 (1992).
- [60] S. Östlund and S. Rommer, Thermodynamic limit of density

- matrix renormalization, *Phys. Rev. Lett.* **75**, 3537 (1995).
- [61] Z. Zhu, D. Sheng, and A. Vishwanath, Doped mott insulators in the triangular lattice hubbard model, *arXiv preprint arXiv:2007.11963* (2020).
- [62] A. E. Trumper, C. J. Gazza, and L. O. Manuel, Quasiparticle vanishing driven by geometrical frustration, *Phys. Rev. B* **69**, 184407 (2004).
- [63] M. Vojta, Spin polarons in triangular antiferromagnets, *Phys. Rev. B* **59**, 6027 (1999).